



MIT Open Access Articles

Tight binding within the fourth moment approximation: Efficient implementation and application to liquid Ni droplet diffusion on graphene

The MIT Faculty has made this article openly available. **Please share** how this access benefits you. Your story matters.

Citation	Los, J., C. Bichara, and R. J. M. Pellenq. "Tight Binding Within the Fourth Moment Approximation: Efficient Implementation and Application to Liquid Ni Droplet Diffusion on Graphene." Physical Review B 84.8 (2011): [12 pages]. ©2011 American Physical Society.
As Published	http://dx.doi.org/10.1103/PhysRevB.84.085455
Publisher	American Physical Society
Version	Final published version
Citable link	http://hdl.handle.net/1721.1/69609
Terms of Use	Article is made available in accordance with the publisher's policy and may be subject to US copyright law. Please refer to the publisher's site for terms of use.

Tight binding within the fourth moment approximation: Efficient implementation and application to liquid Ni droplet diffusion on graphene

J. H. Los,¹ C. Bichara,¹ and R. J. M. Pellenq^{1,2}

¹Centre interdisciplinaire de Nanoscience de Marseille (CINAM), CNRS-UPR 3118, Campus de Luminy, F-13288 Marseille, France

²Department of Civil and Environmental Engineering MIT, 77 Massachusetts Avenue, Cambridge, Massachusetts 02139, USA

(Received 8 February 2011; revised manuscript received 13 May 2011; published 31 August 2011)

Application of the fourth moment approximation (FMA) to the local density of states within a tight binding description to build a reactive, interatomic interaction potential for use in large scale molecular simulations, is a logical and significant step forward to improve the second moment approximation, standing at the basis of several, widely used (semi-)empirical interatomic interaction models. In this paper we present a sufficiently detailed description of the FMA and its technical implications, containing the essential elements for an efficient implementation in a simulation code. Using a recent, existing FMA-based model for C-Ni systems, we investigated the size dependence of the diffusion of a liquid Ni cluster on a graphene sheet and find a power law dependence of the diffusion constant on the cluster size (number of cluster atoms) with an exponent very close to $-2/3$, equal to a previously found exponent for the relatively fast diffusion of solid clusters on a substrate with incommensurate lattice matching. The cluster diffusion exponent gives rise to a specific contribution to the cluster growth law, which is due to cluster coalescence. This is confirmed by a simulation for Ni cluster growth on graphene, which shows that cluster coalescence dominates the initial stage of growth, overruling Oswald ripening.

DOI: [10.1103/PhysRevB.84.085455](https://doi.org/10.1103/PhysRevB.84.085455)

PACS number(s): 31.15.aq, 31.15.bu, 36.40.Sx

I. INTRODUCTION

The interest in modeling finite temperature equilibrium, dynamic, and reactive properties of large systems at the atomic scale with sufficient accuracy has increased considerably in the last decades with the appearance and improvement of various types of (semi-)empirical interatomic potentials that are computationally much more efficient and faster than *ab initio* methods. The (semi-)empirical approaches include Stillinger- and Weber-type models,¹⁻³ (modified) embedded atom methods,⁴⁻⁸ empirical bond order potentials (BOPs),⁹⁻¹⁶ and higher-order, so-called analytical bond order potentials (ABOPs),¹⁷⁻²⁵ which remain closer to tight binding (TB) models building on the works in, for example, Refs. 26-29. It is clear that the qualification “sufficient accuracy” strongly depends on the application. It is generally assumed, and to a certain extent confirmed by experiments, that nowadays state-of-the-art *ab initio* methods are more accurate than (semi-)empirical methods in situations to which the latter models have not been fitted. In fact, a serious difficulty when using a (semi-)empirical model is that it is not so easy to know how accurate it actually is, which undermines its predictive qualities. Normally, such a potential gradually reveals its properties and failures while it is being tested and applied to a variety of systems and conditions for which experimental data are available and/or which allow for comparison with *ab initio* calculations. After that, models can be improved or another model may be selected for a certain application. The fact remains that for many applications empirical models give access to thermodynamic and kinetic properties via simulation for which *ab initio* methods, say within density functional theory (DFT), and even standard TB methods are simply too slow and for which the assumed additional accuracy of these latter methods seems only a matter of details. Of course, there are many other applications which absolutely require an *ab initio* approach.

In the context of the present paper, it is important to mention that the most successful (semi-)empirical, reactive models (i.e., able to describe chemical bond formation and breaking) are essentially rooted in a TB description.³⁰⁻³⁴ In fact, they can be derived starting from the so-called second moment approximation (SMA) to the electronic local density of states (LDOS) at the atomic positions. Usually, the final model takes a purely analytical form. The SMA involves only interactions between atoms within a close neighborhood (sometimes reaching beyond first nearest neighbors) and by this it benefits from the locality in the dependencies of the terms describing the total energy of the system. Here we are paying a first price for such a description, as we know that quantum mechanics is essentially a nonlocal theory. Although most current quantum mechanical computation models also build on certain local approximations, they are clearly less local than the empirical models. Fortunately, for many systems and especially for pure systems the assumption of a local theory is not so bad as it seems for a property like the cohesive energy due to an intrinsic mechanism which strongly favors states for which local charge neutrality is preserved.

While the SMA has been fairly successful for metals, its limitations clearly show up when applying it to covalent systems. For example, for carbon, the large variation in the bond strength between two carbon atoms, including single, double, triple, and conjugated bonds, requires a description which goes beyond nearest neighbors, as is illustrated in Fig. 1. A logical next step to improve the models based on the SMA is to build a model in which the LDOS is treated within the fourth moment approximation (FMA). This approximation stands at the basis of a recently published interaction model for nickel-carbon systems.²⁵ It does not belong to the above-mentioned ABOPs, as the analyticity is lost to a certain extent. In turn, more quantum aspects are preserved, including the explicit evaluation and filling of the LDOS. Retaining the electronic structure up to the fourth moment level would, in

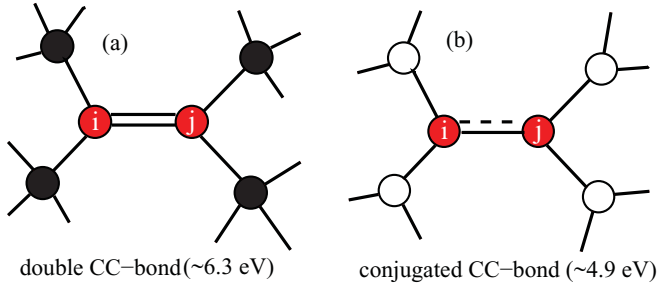


FIG. 1. (Color online) The bond energies of a CC bond between two threefold coordinated carbon atoms i and j depends significantly on the coordinations of the other neighbors, and thus on the second-nearest neighbors. In panel (a) these neighbors are saturated with coordination 4, giving rise to a double CC bond, whereas in panel (b) the environment is sp^2 , like, for example, in graphene.

principle, make it possible to consider electronic (transport) properties and to deal with charge transfer effects, etc. For the description of the energetics of a pure metal, for example, it seems unnecessary to retain the electronic structure up to this level. However, for systems composed of more than one component, such as carbon-nickel systems,²⁵ the importance of such an approximation becomes evident. In particular, it is the lowest-order (simplest) approximation that takes into account both diagonal disorder (difference in on-site energy levels) and off-diagonal disorder (difference in hopping matrix elements). For example, this property seems to be crucial for a proper description of the mixing behavior of transition metal alloys, as has been demonstrated very recently.³⁵

The major aim of this work is to give a basic description of the FMA and its (technical) implications, considering it a natural next step and for certain systems the necessary improvement beyond the so widely used SMA. This analysis directly applies to the model in Ref. 25, being a prototype FMA model, and stands at the basis of a very efficient implementation in a Monte Carlo (MC) simulation code, which we recently realized and of which we will provide the most important ingredients. The code, which gave an improvement in speed by a factor 100 to 2000 with respect to a previous version based on straightforward implementation, shows a linear dependence of the simulation time on the system size (number of atoms). For a system of a few thousand atoms it is several orders of magnitude faster than standard TB, using diagonalization of the TB Hamiltonian matrix, and only up to one order of magnitude slower than SMA-based models. The linear scaling makes it a so-called order- N method, along with previous, alternative order- N methods.^{36–44} It should be noticed, however, that, due to a smaller prefactor, FMA is significantly faster than, for example, the method involving the approximation of the Fermi function by a polynomial of an unavoidable, relatively high order^{41,43} requiring as many moments to be calculated, albeit that the latter method may provide higher accuracy depending on the type of system.

As an example of a simulation study of an interesting and relevant physical problem, which has become feasible with the new code, we used it to simulate the diffusion of liquid Ni clusters on a graphene sheet. Here our aim is to investigate

the dependence of the cluster diffusion constant on its size N (number of Ni atoms in the cluster), in order to establish whether there is a power law behavior $D_N \propto N^{-\alpha}$ and, if so, to extract the exponent α .

The fact that there is no true time scale in MC simulation has sometimes led to the idea that MC simulation cannot be used for studying dynamical processes. However, as has been shown in, for example, Ref. 45, under certain conditions one can assume that MC “time,” taking it as the average number of displacement attempts per atom, is proportional to the real time except for short time scales. In the present application, keeping the acceptance rate for the MC displacement trials constant is enough to recover the essential features of diffusion in our MC simulations. It is indeed not possible to determine (directly) absolute values of D_N , but this does not hinder the study of the size dependence of D_N at a fixed temperature T . An estimate of absolute values can be obtained by choosing a suitable reference process with a (experimentally) known time scale like the atomic (self-)diffusion, as we will do.

The value of the above-mentioned exponent α is important for the contribution of cluster coalescence to cluster growth on a two-dimensional (2D) substrate, as a second mechanism besides Oswald ripening. For Oswald ripening the (average) linear cluster size grows as t^β with $\beta = 1/3$ if diffusion is the rate limiting process⁴⁶ and $\beta = 1/2$ when surface kinetics is the slowest process.⁴⁷ For compact, 3D clusters this would give rise to a contribution $\langle N(t) \rangle \propto t^{3\beta}$ to the cluster growth law. For cluster coalescence, an analytical solution⁴⁸ predicts the average density of clusters to behave as $\langle \rho_{cl}(t) \rangle \propto t^{-3/(3+\gamma)}$, implying $\langle N(t) \rangle \propto t^{3/(3+\gamma)}$ where γ is the exponent in the diffusion constant power law dependence $D(r) \propto r^{-\gamma}$ on the cluster radius r . So in any case, since normally $\gamma > 0$ implying $3\beta > 3/(3+\gamma)$, Oswald ripening will be the fastest, and thus prevailing, growth process for large times. However, for small and intermediate times scales cluster coalescence may contribute significantly to the growth, depending on the kinetic prefactors. The two growth mechanisms together and using $\alpha = \gamma/3$ give rise to

$$\langle N(t) \rangle = N_0 + K_{CC}t^{1/(1+\alpha)} + K_{OR}t^{3\beta}, \quad (1)$$

predicting a crossover in the prevailing mechanism. K_{CC} and K_{OR} are the kinetic constants for cluster coalescence and Oswald ripening, respectively.

While the diffusion of solid clusters has been studied frequently in the past, both experimentally^{49–53} and theoretically,^{54–61} investigations of liquid cluster diffusion are limited to only a few.^{62,63}

Most of the works on solid clusters focus on 2D clusters, epitaxially attached to the substrate, for which the diffusion is quite slow, of the order of 10^{-17} cm²/s, and takes place by single-atom events. Different mechanisms were identified, giving rise power law dependencies ranging from $D(r) \propto 1/r^3$ for periphery diffusion to $D(r) \propto 1/r^2$ and $D(r) \propto 1/r$ for respectively a correlated and an uncorrelated evaporation and condensation mechanism (see Ref. 56), r being the 2D cluster radius now. However, these single-atom mechanisms cannot explain the very fast diffusion of the order of 10^{-8} cm²/s at room temperature reported in Refs. 51 and 52. A plausible explanation for this fast diffusion is given in Ref. 60 in which

it is shown by simulations based on Lennard-Jones (LJ) interactions for 3D clusters on a substrate, that is, the partial wetting case, that the diffusion constant can increase by many orders of magnitude when changing from a situation in which the cluster and the substrate lattice parameters are commensurate to a situation in which they are incommensurate. The exponent α in the power law $D_N \propto N^{-\alpha}$ was found to vary between $\alpha = 2/3$ for the incommensurate case with a Brownian-like mechanism to $\alpha = 1.4$ for the small mismatch case with a hoppinglike mechanism. In both mechanisms the cluster moves as a whole, contrary to the case of single-atom mechanisms.

It is not so clear to what extent 3D liquid cluster diffusion on a substrate, as considered here, is qualitatively different from that of 2D and/or 3D solid clusters. In the simulation study of Ref. 62 of a 3D liquid gold (Au) cluster diffusion on an amorphous frozen-in substrate, an exponent $\alpha = 1.3$ was found for the smaller clusters, but the largest cluster (555 atoms) was found to diffuse even slower than predicted by this power law. Here a rolling-like, or rather a stick-and-roll, mechanism was identified which to some extent corresponds to the stick-and-glide mechanism observed in the small mismatch case of solid cluster diffusion. This could explain the similarity in the power law exponents, that is, 1.3 versus 1.4. In the incommensurate case the energy barriers for diffusion are much smaller, giving rise to a random walk mechanism. It seems that the substrate properties used in Ref. 62, being amorphous and static, might have been decisive for the diffusion mechanism. Apparently, the cluster is able to find relatively stable positions on the surface, with a relatively low escape probability. In our simulations the substrate is crystalline and its atoms are allowed to move. While the (111) surface of Ni matches almost perfectly with graphene, one expects no particular lattice matching for a liquid cluster. In addition, the effect of energy barriers is reduced at high temperature. This makes us expect a power law behavior similar to that for the incommensurate solid cluster case, with $\alpha = 2/3$, that is, a D_N which is inversely proportional to the contact area.

In the next two sections we give a description of the TB model within the fourth moment approximation (TBFMA), such as it is applied in Ref. 25, and all important implications and ingredients for constructing a fast MC simulation code. Section IV is devoted to its application to liquid Ni cluster diffusion and growth on graphene, while Sec. V contains a summary and conclusions.

II. TIGHT BINDING WITHIN THE FOURTH MOMENT APPROXIMATION

The total energy E of the TBFMA model in Ref. 25 is the sum of atomic energies E_i :

$$E = \sum_{i=1}^{N_{at}} E_i = \sum_i (E_{R,i} + E_{C,i}), \quad (2)$$

where $E_{R,i}$ and $E_{C,i}$ are the atomic repulsive and cohesive energies for atom i , respectively, and N_{at} is the number of atoms in the system. The repulsive energy of atom i reads

$$E_{R,i} = F \left(\sum_j V_R(r_{ij}) \right), \quad (3)$$

where $V_R(r_{ij})$ is a repulsive pair potential and F is an embedding function to extend the transferability of the model for different coordination environments. A finite cutoff distance at which $V_R(r_{ij})$ smoothly vanishes limits the sum over j to atoms within this distance from atom i . The atomic, cohesive energy is given by

$$\begin{aligned} E_{C,i} &= 2 \int_{-\infty}^{E_F} (E - \epsilon_i) n_i(E) dE \\ &= 2 \int_{-\infty}^{E_F} (E - \epsilon_i) \sum_{\lambda} n_{i,\lambda}(E) dE, \end{aligned} \quad (4)$$

where the prefactor 2 accounts for the two spin states, E_F is the Fermi energy, ϵ_i is the average orbital energy per electron for an isolated atom i , and $n_i(E)$ is the LDOS of atom i , consisting of a sum of contributions $n_{i,\lambda}(E)$ from the different, involved orbital groups or bands λ (e.g., $2s$ and $2p$ for carbon), forming the basis of orbitals. Within the TB description the LDOS for band λ is defined as

$$\begin{aligned} n_{i,\lambda}(E) &= -\frac{n_{\lambda}}{\pi} \lim_{\epsilon \rightarrow 0} \text{Im} \left(\frac{1}{n_{\lambda}} \sum_m^{n_{\lambda}} \langle i\lambda_m | G(z) | i\lambda_m \rangle \right) \\ &\equiv -\frac{n_{\lambda}}{\pi} \lim_{\epsilon \rightarrow 0} \text{Im} \hat{G}_{ii,\lambda\lambda}(z), \end{aligned} \quad (5)$$

where the sum runs over the n_{λ} orbitals λ_m in band λ (e.g., $2p_x$, $2p_y$, and $2p_z$ for the $2p$ band yielding $n_{\lambda} = 3$) and where $G(z) = (zI - H_{TB})^{-1}$ is the Green's function operator with $z = E + i\epsilon$ and H_{TB} the Slater-Koster⁶⁴ TB Hamiltonian. Employing Lanczos tridiagonalization of H_{TB} with the appropriate initial Lanczos vector and using a recursive relation for the cofactors of a tridiagonal matrix, $\hat{G}_{ii,\lambda\lambda}(z)$ can be rewritten as a continued fraction (CF) expansion²⁷:

$$\hat{G}_{ii,\lambda\lambda}(z) = \frac{1}{z - a_1^{i\lambda} - \frac{b_1^{i\lambda}}{z - a_2^{i\lambda} - \frac{b_2^{i\lambda}}{z - a_3^{i\lambda} - \frac{b_3^{i\lambda}}{\dots}}}}, \quad (6)$$

where the continued fraction coefficients (CFCs) $a_m^{i\lambda}$ and $b_m^{i\lambda} = (\beta_m^{i\lambda})^2$ are the diagonal and the squares of the off-diagonal elements of the Lanczos tridiagonal matrix, respectively.

Alternatively, $\hat{G}_{ii,\lambda\lambda}(z)$ can be expanded as

$$\hat{G}_{ii,\lambda\lambda}(z) = \frac{1}{n_{\lambda}} \sum_m^{n_{\lambda}} \langle i\lambda_m | (zI - H_{TB})^{-1} | i\lambda_m \rangle = \sum_{n=0}^{\infty} \frac{\mu_n^{i\lambda}}{z^{n+1}}, \quad (7)$$

where $\mu_n^{i\lambda} = (1/n_{\lambda}) \sum_m \langle i\lambda_m | H_{TB}^n | i\lambda_m \rangle$ represents the n th moment for atom i and band λ . The moment $\mu_n^{i\lambda}$ involves all closed hopping pathways consisting of n nearest-neighbor hoppings and/or onsite loops beginning and ending on a λ_m orbital of atom i (see Fig. 1). There is a one-to-one correspondence between the moments and the CFCs. The CF expansion is much more suitable for evaluation of the LDOS than the moments expansion and normally the CFCs can be calculated accurately using the Lanczos algorithm. However, an efficient implementation of the TBFMA model in a MC code requires the moments, as will be shown in Sec. III A. Since the moments $\mu_n^{i\lambda}$ rapidly diverge for increasing n , contrary to the CFCs, naive calculation of the CFCs from the moments can easily lead to large inaccuracies in the

CFCs. This problem can be solved by using the following numerically stable algorithm, in which the CFCs $a_n^{i\lambda}$ and $b_n^{i\lambda}$ for $n = 1, \dots, m/2$ (m even) are calculated from the first m moments μ_i ($i = 1, \dots, m$) iteratively by⁶⁵

$$\begin{aligned} v_1^{(n)} &= -\mu_1^{(n)}, \\ v_i^{(n)} &= -\mu_i^{(n)} - \sum_{j=1}^{i-1} \mu_{i-j}^{(n)} v_j^{(n)} \quad \text{for } i = 2, \dots, m - 2(n-1), \\ a_n^{i\lambda} &= -v_1^{(n)}, \quad b_n^{i\lambda} = -v_2^{(n)} \\ \mu_i^{(n+1)} &= -v_{i+2}^{(n)} / b_n^{i\lambda} \quad \text{for } i = 1, \dots, m - 2n, \end{aligned} \quad (8)$$

for $n = 1, \dots, m/2$ with $\mu_i^{(1)} = \mu_i$ ($i = 1, \dots, m$).

In principle there are several options to terminate the CF expansion. The simplest option would be to truncate it at some level n by just taking $b_n^{i\lambda} = 0$. This leads to a LDOS containing only Dirac peaks, maximally n . For the application to bulk phases, a more realistic LDOS, containing an energy band, is obtained by taking the CFCs constant beyond a certain level. In particular, within the TBFMA model of Ref. 25 all CFCs beyond $n = 2$ are taken constant and equal to $a_n^{i\lambda} = a_2^{i\lambda}$ and $b_n^{i\lambda} = b_2^{i\lambda}$. Eventually, this leads to a relatively simple analytical expression for the LDOS, as described in Sec. III B. The four coefficients $a_1^{i\lambda}$, $a_2^{i\lambda}$, $b_1^{i\lambda}$, and $b_2^{i\lambda}$ require only the first four moments and are readily calculated in two steps of the algorithm in Eq. (8).

Another approximation applied in the TBFMA model for C-Ni systems of Ref. 25 is that charge transfer is neglected by applying the constraint

$$Z_i = 2 \int_{-\infty}^{E_{F,i}} n_i(E) dE, \quad (9)$$

where $E_{F,i}$ is the highest occupied level of the LDOS of atom i and Z_i is the number of valence electrons for atom i in the chosen basis of orbitals for that atom. For C, described within the $(2s, 2p)$ basis, $Z_i = 4$, whereas $Z_i = 8$ for Ni, described within the $3d$ basis. The neglect of charge transfer is a reasonable approximation for C-Ni systems,²⁵ but not a necessary requirement for the analytical analysis in Sec. III B.

III. EFFICIENT IMPLEMENTATION

A. (Re)calculating moments in an efficient way

For standard MC simulation, in order to calculate the change in the total energy for a new trial configuration generated by a random displacement of a randomly chosen atom i , only certain moments of atoms up to second neighbors of atom i need to be recalculated. To facilitate the discussion here, let us consider a move which does not cause a coordination change (no cutoff radius is crossed). After such a move, in principle all four moments for atom i change. For the nearest neighbors j of atom i , the second, the third, and the fourth moments change. However, for a second-nearest neighbor k of atom i , only the fourth moment changes (see Fig. 2). In addition, the change of the fourth moment of such an atom k is only due to the change of a very limited number of closed hopping pathways, namely, only those pathways which pass by the displaced atom i . Also for the first nearest neighbors j , only a fraction of the pathways pass by atom i and contribute

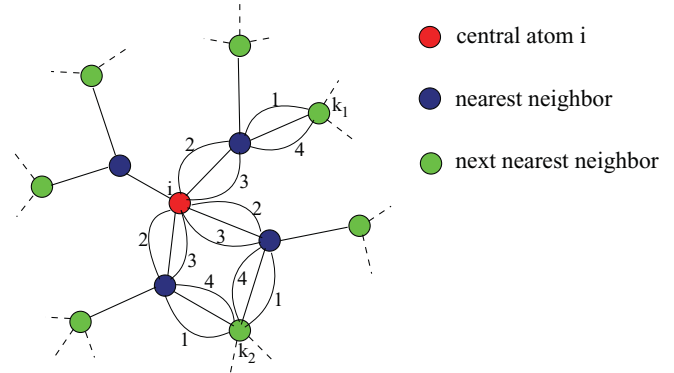


FIG. 2. (Color online) Schematic representation of all the atoms whose energies change after a displacement of the central atom i . The hopping pathways from i to a second neighbor k_1 can be reused to compute the change in the fourth moment of the atom k_1 , as these are the only pathways for atom k_1 which change after a displacement of the atom i . For atom k_1 this includes only one pathway. For atom k_2 , we have drawn all pathways that change and that start and end on k_2 , which include four pathways in this case. All the possible changed pathways are automatically included in the algorithm presented in Table I.

to the changes in the second, third, fourth moment. To exploit these facts we designed a very efficient and relatively simple algorithm for updating the moments after a move, which is outlined in Table I.

In the description in Table I, H_{ij} represents a $(n_i \times n_j)$ matrix block of the TB hamiltonian. For $j = i$, H_{ij} is diagonal and contains the average band energy levels, while for $j \neq i$, H_{ij} contains the probabilities for hopping from each of the n_i orbitals of atom i to each of the n_j orbitals of atom j . H_{ij}^T and H_{ik}^{2T} are just the transposed matrices of H_{ij} and H_{ik}^2 , respectively, and $D[\dots]$ stands for “diagonal of”. The n_i components of the vector $\mu_{i,n}$ contain the n th moment for each orbital on atom i . In particular, the change of the fourth moment of all second-nearest neighbors can be computed very efficiently from the matrix blocks $H_{ki}^2 = H_{ik}^{2T}$ which have already been computed in the recalculation of the moments of the central atom i !

B. Analytic integration of the local density of states

Within the FMA, the integrated, normalized LDOS for band λ at atom i , $I_{i\lambda}$, reads

$$\begin{aligned} I_{i\lambda}(E_{F,i}) &= -\frac{1}{\pi} \lim_{\epsilon \rightarrow 0} \text{Im} \int_{-\infty}^{E_{F,i}} \hat{G}_{ii,\lambda\lambda}(z) \\ &= -\frac{1}{\pi} \lim_{\epsilon \rightarrow 0} \text{Im} \int_{-\infty}^{E_{F,i}} \frac{dE}{z - a_1^{i\lambda} - \frac{b_1^{i\lambda}}{z - a_2^{i\lambda} - b_2^{i\lambda} \Sigma^{i\lambda}(z)}}, \end{aligned} \quad (10)$$

where $\Sigma^{i\lambda}(z) = 1/[z - a_2^{i\lambda} - b_2^{i\lambda} \Sigma^{i\lambda}(z)]$. It holds that $I_{i\lambda}(\infty) = 1$ by construction.

Allan *et al.*⁶⁶ have found an analytical solution for the general variant of the integral (10) and the corresponding energy integral with a CF expansion of arbitrary length terminated by a $\Sigma(z)$ of the above-described form. It was

TABLE I. Computation steps for efficient recalculation of the moments after a displacement of an atom i in MC simulation. Note that the quantities $\delta\mu_{k,m}$, $\delta\mu_{j,m}$ ($m = 2,3,4$) include only a part of closed hopping pathways for atoms k and j , namely, only the ones that change. The quantities with and without prime indexes indicate the values after and before the displacement of atom i . The terms “nn” and “nnn” stand for nearest and next-nearest neighbors respectively.

(1) Atom i	all moments change
– Compute: $H_{ik}^2 = \sum_j H_{ij}H_{jk}$	for $k = i$, k nn of i and k nnn of i
– Compute:	
$\bar{\mu}'_{i,1} = D[H_{ii}]$	
$\bar{\mu}'_{i,2} = D[\sum_j H_{ij}H_{ji}] = D[\sum_j H_{ij}H_{ij}^T]$	
$\bar{\mu}'_{i,3} = D[\sum_j H_{ij}^2H_{ji}] = D[\sum_j H_{ij}^2H_{ij}^T]$	
$\bar{\mu}'_{i,4} = D[\sum_k H_{ik}^2H_{ki}^2] = D[\sum_k H_{ik}^2H_{ik}^{2T}]$	
(2) Next-nearest neighbors k of atom i	only $\bar{\mu}_{k,4}$ changes
– Compute: $\delta\bar{\mu}'_{k,4} = D[H_{ki}^2H_{ik}^2] = D[H_{ik}^{2T}H_{ik}^2]$	
– Compute: $\bar{\mu}'_{k,4} = \bar{\mu}_{k,4} + \delta\bar{\mu}'_{k,4} - \delta\bar{\mu}_{k,4}$	
(3) Nearest neighbors j of atom i	$\bar{\mu}_{j,2}$, $\bar{\mu}_{j,3}$, and $\bar{\mu}_{j,4}$ change
– Compute: $H_{jj'}^2 = \sum_k H_{jk}H_{kj'}$	only for $j' = i$ and j' nn of i
– Compute: $\delta\bar{\mu}'_{j,2} = D[H_{ji}H_{ij}] = D[H_{ij}^T H_{ij}]$	
– Compute: $\delta\bar{\mu}'_{j,3} = D[\sum_{j'} H_{jj'}^2 H_{j'j}] = D[\sum_{j'} H_{jj'}^2 H_{j'j}^T]$	$j' = i, j$ or (j' nn of j and of i) !
– Compute: $\delta\bar{\mu}'_{j,4} = D[\sum_{j'} H_{jj'}^2 H_{j'j}^2] = D[\sum_{j'} H_{jj'}^2 H_{j'j}^{2T}]$	$j' = i, j$ or j' nn of i !
– Compute: $\bar{\mu}'_{j,m} = \bar{\mu}_{j,m} + \delta\bar{\mu}'_{j,m} - \delta\bar{\mu}_{j,m}$	$m = 2,3,4$

shown that these solutions allow a much faster and more accurate evaluation of the relevant quantities in comparison to numerical integration. We have worked out the solutions for the case of the FMA, which allows additional simplifications and explicit analytical expressions for the integrals in terms of the four CFCs, as given below.

It is convenient to apply the following change of variable:

$$z' = \frac{z - a_2^{i\lambda}}{\sqrt{b_2^{i\lambda}}} \Rightarrow z = \sqrt{b_2^{i\lambda}} z' + a_2^{i\lambda}, \quad (11)$$

by which Eq. (10) transforms into

$$I'_{i\lambda}(E'_{F,i\lambda}) = -\frac{1}{\pi} \lim_{\epsilon \rightarrow 0} \text{Im} \int_{-\infty}^{E'_{F,i\lambda}} \frac{dE'}{z' - a_1^{i\lambda'} - b_1^{i\lambda'} \Sigma'(z')}, \quad (12)$$

where $\Sigma'(z') = 1/[z' - \Sigma'(z')]$, $a_1^{i\lambda'} = a_1^{i\lambda} - a_2^{i\lambda}$, $b_1^{i\lambda'} = b_1^{i\lambda}/b_2^{i\lambda}$, and $E'_{F,i\lambda} = (E_{F,i} - a_2^{i\lambda})/\sqrt{b_2^{i\lambda}}$. In fact, in the transformed CF expansion, $a_2^{i\lambda'} = 0$ and $b_2^{i\lambda'} = 1$. Hence, by this variable change, consisting of a scaling and a shift of the energy, we have obtained a simplified CF expansion with only two parameters, $a_1^{i\lambda'}$ and $b_1^{i\lambda'}$. The Eq. (9) to find $E_{F,i}$ can be rewritten in terms of the transformed integral as

$$Z_i = 2 \sum_{\lambda} n_{\lambda} I_{i\lambda}(E_{F,i}) = 2 \sum_{\lambda} n_{\lambda} I'_{i\lambda}(E'_{F,i\lambda}). \quad (13)$$

Solving Eq. (13) for $E'_{F,i}$ (and $E_{F,i}$) with the analytical expressions for $I'_{i\lambda}$ given below, has to be done numerically with an appropriate method, such as Newton-Raphson and/or bisection. Once we have $E'_{F,i}$, the cohesive energy for atom

i can be determined by the energy integral (4), which after transformation becomes

$$E_{C,i} = 2 \sum_{\lambda} n_{\lambda} \left(\sqrt{b_2^{i\lambda}} I'_{E,i\lambda}(E'_{F,i\lambda}) + (a_2^{i\lambda} - \epsilon_i) I'_{i\lambda}(E'_{F,i\lambda}) \right), \quad (14)$$

where

$$I'_{E,i\lambda}(E'_{F,i\lambda}) = -\frac{1}{\pi} \lim_{\epsilon \rightarrow 0} \text{Im} \int_{-\infty}^{E'_{F,i\lambda}} \frac{E' dE'}{z' - a_1^{i\lambda'} - b_1^{i\lambda'} \Sigma'(z')}. \quad (15)$$

So to find $E_{C,i}$ we have to perform the integrals $I'_{i\lambda}(E'_{F,i\lambda})$ and $I'_{E,i\lambda}(E'_{F,i\lambda})$, expressed in terms of $a_1^{i\lambda'}$, $b_1^{i\lambda'}$, and $E'_{F,i\lambda}$. In the further description of this problem we drop the prime indexes and superscript/subscript $i\lambda$ for convenience.

Solving the quadratic equation for Σ , the integrand of Eq. (12) can be rewritten as

$$\hat{G}(E) = \frac{2}{(2 - b_1)z - 2a_1 \mp b_1 \sqrt{z^2 - 4}} \equiv \frac{2}{D_{\mp}(z)}, \quad (16)$$

where $D_{\mp}(z) \equiv (2 - b_1)z - 2a_1 \mp b_1 \sqrt{z^2 - 4}$, the signs \mp corresponding to the two roots $\Sigma_{\pm} = (z \pm \sqrt{z^2 - 1})/2$. For real $z = E$, Eq. (16) can be worked out to

$$\hat{G}(E) = \frac{(2 - b_1)E - 2a_1 - b_1 S \sqrt{|4 - E^2|}}{2 \left[(1 - b_1)E^2 - a_1(2 - b_1)E + a_1^2 + b_1^2 \right]}, \quad (17)$$

where $S = i$ for $|E| \leq 2$, $S = -1$ for $E < -2$, and $S = 1$ for $E > 2$, the signs of S being chosen such that the LDOS is always positive. For energies within the interval $-2 \leq E \leq 2$, $\hat{G}(E)$ has a continuous imaginary part, giving rise to an energy band. Other contributions to the LDOS may come from poles on the real axis giving rise to Dirac peaks. Normally, Dirac peaks only occur for strongly distorted local configurations. One should be careful with the interpretation of the details of the LDOS, like the Dirac peaks (normally indicating singular states), since the LDOS within the TBFMA is only an approximation. Fortunately, integrated quantities like the total energy are not so sensitive for these details.

From Eq. (16) it readily follows that any pole z_i is a solution of the equation

$$z^2 = 4 + \frac{1}{b_1^2} [(2 - b_1)z - 2a_1]^2, \quad (18)$$

which immediately shows that for a real pole $z_i = E_i$ it holds that $|E_i| \geq 2$; that is, real poles are at the edge or outside the band. However, a real root E_i of Eq. (18) is not always a pole. As Eq. (18) was obtained after multiplying numerator and denominator of Eq. (17) with D_+ (D_-), E_i is only a pole if $D_+(E_i) \neq 0$ [$D_-(E_i) \neq 0$]. It also follows from Eq. (18) that for any value of a_1 , there is always a b_1 value for which there is a root $E_i = -2$ at the lower band edge and a b_1 value yielding a root $E_i = 2$ at the upper band edge. Indeed, substitution of $E_i = -2$ into Eq. (18) yields $b_1 = 2 + a_1$, whereas substitution of $E_i = 2$ leads to $b_1 = 2 - a_1$. Moreover, a negative root E_i of Eq. (18) is only a pole when $b_1 > 2 + a_1$, whereas a positive E_i is only a pole when $b_1 > 2 - a_1$. The general, complex roots of Eq. (18) for $b_1 \neq 1$ are

$$z_i = \frac{a_1(2 - b_1) - (-1)^i b_1 \sqrt{4b_1 - 4 + a_1^2}}{2(1 - b_1)}, \quad (19)$$

for $i = 1, 2$, showing that the LDOS may only contain pole contributions (Dirac peaks) for $b_1 > 1 - a_1^2/4$.

The coefficient a_1 describes the asymmetry of the band. Indeed, for $a_1 = 0$, we have $\text{Im}[\hat{G}(-E + i\epsilon)] = \text{Im}[\hat{G}(E + i\epsilon)]$, so that $n(E) \equiv -1/\pi \text{Im}\hat{G}(E)$ is symmetric with respect

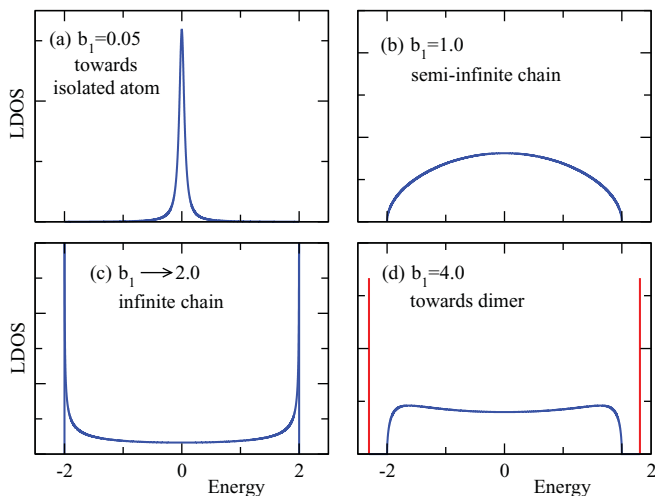


FIG. 3. (Color online) Local density of states for $a_1 = 0$ (symmetric case) and four values of b_1 .

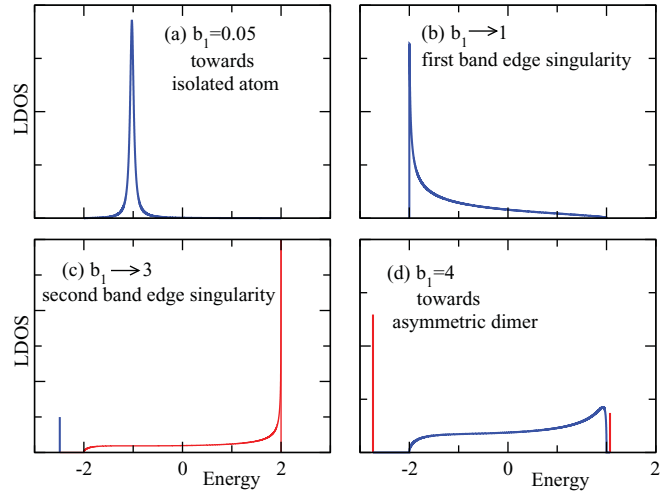


FIG. 4. (Color online) Local density of states for $a_1 = -1$ and four values of b_1 .

to $E = 0$. The coefficient b_1 controls the tendency to form a band gap. Examples of $n(E)$ for symmetric and asymmetric bands are shown in Figs. 3 and 4, respectively. Figure 5 gives a graphical representation of the properties of $n(E)$ as a function of b_1 for the symmetric and an asymmetric case with $a_1 = -1$. For $b_1 < 2 - |a_1|$ there are no Dirac peak contributions to the LDOS. For $2 - |a_1| \leq b_1 \leq 2 + |a_1|$ the LDOS contains one Dirac peak and for $b_1 > 2 + |a_1|$, it contains two Dirac peaks, as also shown in Fig. 6. The quantities W_{p1} and W_{p2} in Fig. 5 are the electronic weight factors (residues) of the poles. In the limit of very large b_1 , the band contribution vanishes and the LDOS consists of just two Dirac peaks corresponding to the two poles with $W_{p1} + W_{p2}$ tending to one. This situation can occur for a dimer.

Following Allan *et al.*,⁶⁶ the band contribution I_b to $I = I_b + I_p$ can be found to be

$$I_b(E_F) = \frac{1}{\pi} \int_{-2}^{E_F} \frac{b_1 \sqrt{4 - E^2}}{2(1 - b_1)(E - z_1)(E - z_2)} dE = \sum_{i=1}^2 c_i I_{b,i}(E_F), \quad (20)$$

where

$$c_i = \frac{-(-1)^i}{2\pi \sqrt{4b_1 - 4 + a_1^2}} \quad (21)$$

and

$$I_{b,i}(E_F) = 2 \cos(t_F) - z_i \left(\frac{\pi}{2} + t_F \right) + \sqrt{4 - z_i^2} \times \left[\log \left(\frac{u_i^+ + 1}{u_i^- + 1} \right) - \log \left(\frac{u_F - u_i^+}{u_F - u_i^-} \right) \right], \quad (22)$$

with $t_F = \arcsin(E_F/2)$, $u_F = \tan(t_F/2)$, and z_i ($i = 1, 2$) given by Eq. (19) and where u_i^\pm are the roots of the equation $u^2 - (4/z_i)u + 1 = 0$, reading

$$u_i^\pm = \frac{2 \pm \sqrt{4 - z_i^2}}{z_i}. \quad (23)$$

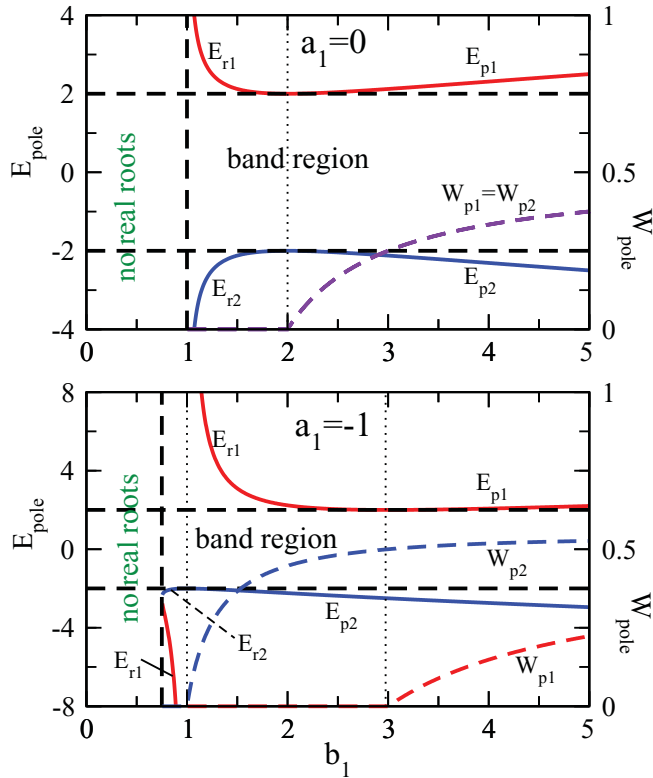


FIG. 5. (Color online) Graphical representation of the LDOS properties as a function of the parameter b_1 for the symmetric case ($a_1 = 0$, top graph) and a nonsymmetric case ($a_1 = -1$, bottom graph). The energies of real roots E_{r_i} of the denominator in Eq. (17) and the real poles E_{p_i} are indicated on the left vertical axis, whereas the corresponding weight factors W_{p_i} (residues) are given on right vertical axis. For $a_1 = 0$, both roots become poles for $b_1 > 2 - a_1 = 2$. For $a_1 = -1$, E_{r_1} becomes a pole E_{p_1} for $b_1 > 2 - a_1 = 3$, whereas E_{r_2} becomes a pole E_{p_2} for $b_1 > 2 + a_1 = 1$.

The imaginary parts of both complex logarithms in Eq. (22) have to be taken within the interval $[0, 2\pi)$.

There are two cases where the evaluation of I_b by the above equations becomes numerically unstable. The first case is when a root z_i becomes very large due to a b_1 value close to one. Then, for the corresponding $I_{b,i}$ both the second and the third term on the right-hand side of Eq. (22) diverge, leading to inaccuracy in the sum of them, knowing that the sum remains finite since $I_b(E_F) \leq 1$ by construction. The second problematic case for similar reasons occurs when c_i diverges for b_1 tending $1 - a_1^2/4$. In MC simulation, especially at high temperature where the domain of accessible CFC values increases, these situations unavoidably occur so that one has to deal with it rigorously. We solved these difficulties in a practical way by bridging the parameter intervals, which cause troubles with linear interpolations. For example, for b_1 within the interval $[b_{1,\min}, 1]$, with $b_{1,\min}$ close to 1 we calculate $I_{b,i}$ as

$$I_{b,i}(b_1; E_F) = \frac{1 - b_1}{1 - b_{1,\min}} I_{b,i}(b_{1,\min}; E_F) + \frac{b_1 - b_{1,\min}}{1 - b_{1,\min}} I_{b,i}(1; E_F), \quad (24)$$

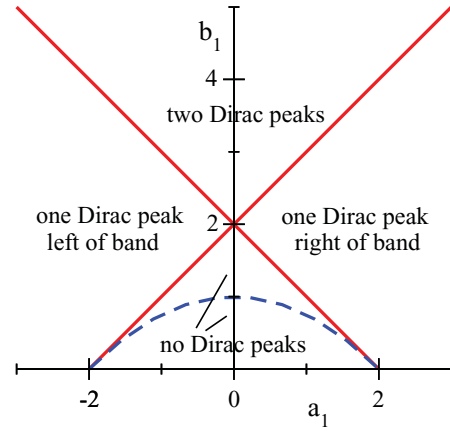


FIG. 6. (Color online) Domains in the parameter space spanned by the transformed CF coefficients a_1 and b_1 for which the LDOS contains 0, 1, and 2 Dirac peaks. In the domain where it contains 2 Dirac peaks, there is one at the left and one at the right side of the band. In the domain enclosed by the dashed line and the a_1 -axis the roots of Eq. (18) are complex.

where $I_{b,i}(b_{1,\min}; E_F)$ and $I_{b,i}(1; E_F)$ are the band integrals for $b_1 = b_{1,\min}$ and $b_1 = 1$, respectively. Typically, a value of $b_{1,\min} = 0.975$ is enough to avoid numerical problems. Strictly speaking, this interpolation introduces kinks in the energy curves, which would be a problem for molecular dynamics (MD) simulations requiring continuity of the derivative of the energy. However, for the MC implementation considered here it is not a problem. Moreover, in practice, within the mentioned small parameter intervals, the kinks are so weak that they cannot or can hardly be detected.

The case $b_1 = 1$ (and $a_1 \neq 0$) is a special case, where the denominator of $\hat{G}(E)$ is a linear function of E and has one, real root equal to $E_1 = (a_1^2 + 1)/a_1$, implying $|E_1| \geq 2$. For $a_1 > 0$, $E_1 \geq 2$ and is only a pole when $a_1 > 1$, whereas for $a_1 < 0$, $E_1 \leq -2$ and is only a pole when $a_1 < -1$. In Eq. (20), now the most right-hand side contains only one term, $c_1 I_{b,1}$, instead of two with $c_1 = -1/(2\pi a_1)$ and $I_{b,1}$ given by Eq. (22) for $i = 1$ with $z_1 = E_1$, u_1^\pm from Eq. (23), and t_F and u_F as before.

An even more special and rare case occurs when $b_1 = 1$ and $a_1 = 0$. In that case,

$$I_b(E_F) = \frac{1}{2\pi} \int_{-2}^{E_F} \sqrt{4 - E^2} dE = \frac{1}{2\pi} [\pi + 2t_F + \sin(2t_F)]. \quad (25)$$

The pole contribution, I_p , to the integrated density of states, $I = I_b + I_p$, is given by

$$I_p(E_F) = \sum_{i=1}^{N_p} f_{ip} W_{pi} \Theta(E_F - E_{pi}), \quad (26)$$

where Θ is Heaviside step function, N_p (1 or 2) is the number of real poles, $f_{ip} \in [0, 1]$ is a filling factor, E_{pi} is the energy of the pole, and W_{pi} its weight factor. For $E_F > E_{pi}$, the filling factor $f_{pi} = 1$, but when $E_F = E_{pi}$ only part of the pole level

may be filled so that $f_{pi} \leq 1$ in that case. Unless $b_1 = 1$, $W_{pi}(i = 1, 2)$ is given by

$$W_{pi} = \frac{2a_1 - (2 - b_1)E_{pi} + b_1 S \sqrt{E_{pi}^2 - 4}}{(-1)^i 2b_1 \sqrt{4b_1 - 4 + a_1^2}}, \quad (27)$$

whereas for $b_1 = 1$ and $|a_1| > 1$, that is, a case with a single Dirac peak, W_{p1} is equal to

$$W_{p1} = \frac{a_1^2 - 1}{a_1^2}. \quad (28)$$

Unless $b_1 = 1$ and $a_1 = 0$, the band and pole contributions to the energy integral $I_E = I_{E,b} + I_{E,p}$ are given by

$$I_{E,b}(E_F) = \sum_{i=1}^{N_r} c_i [\pi + 2t_F + \sin(2t_F) + z_i I_{b,i}(E_F)], \quad (29)$$

with N_r (1 or 2) the number of (complex) roots of Eq. (18) and

$$I_{E,p}(E_F) = \sum_{i=1}^{N_p} f_{pi} W_{pi} E_{pi} \Theta(E_F - E_{pi}), \quad (30)$$

respectively. For $b_1 = 1$ and $a_1 = 0$, there is only a band contribution, which is equal to

$$I_{E,b}(E_F) = \frac{1}{2\pi} \int_{-2}^{E_F} E \sqrt{4 - E^2} dE = -\frac{4}{3\pi} \cos^3(t_F). \quad (31)$$

There are two other special cases which have not been considered so far. In nontransformed coefficients, these cases are $b_1^{i\lambda} = 0$ and $b_2^{i\lambda} = 0$, corresponding to a free atom and a dimer, respectively. In these two cases the transformation (11) is useless and impossible, respectively, and the cohesive energy should be calculated directly without this transformation. For $b_1^{i\lambda} = 0$, the contribution from band λ to the LDOS consists of just one Dirac peak due to a pole at $E = a_1^{i\lambda}$. Using $n_{i\lambda}(E) = -(1/\pi) \text{Im}[1/(E + i\epsilon - a_1^{i\lambda})] = \delta(E - a_1^{i\lambda})$ for $\epsilon \rightarrow 0$, we find

$$\begin{aligned} I_{i\lambda}(E_{F,i}) &= f_{i\lambda} \Theta(E_{F,i} - a_1^{i\lambda}) \quad \text{and} \\ I_{E,i\lambda}(E_{F,i}) &= f_{i\lambda} a_1^{i\lambda} \Theta(E_{F,i} - a_1^{i\lambda}), \end{aligned} \quad (32)$$

with $f_{i\lambda} \in [0, 1]$ a filling factor as before. For $b_2^{i\lambda} = 0$ (and $b_1^{i\lambda} \neq 0$), $n_{i\lambda}(E)$ contains two Dirac peaks at $E_{\pm} = [a_1^{i\lambda} + a_2^{i\lambda} \pm \sqrt{(a_1^{i\lambda} - a_2^{i\lambda})^2 + 4b_1^{i\lambda}}]/2$ and we find

$$\begin{aligned} I_{i\lambda}(E_{F,i}) &= \sum_{\pm} f_{i\lambda}^{\pm} W_{i\lambda}^{\pm} \Theta(E_{F,i} - E_{\pm}) \quad \text{and} \\ I_{E,i\lambda}(E_{F,i}) &= \sum_{\pm} E_{\pm} f_{i\lambda}^{\pm} W_{i\lambda}^{\pm} \Theta(E_{F,i} - E_{\pm}), \end{aligned} \quad (33)$$

with $W_{i\lambda}^{\pm} = \pm(E_{\pm} - a_2^{i\lambda})/(E_{+} - E_{-})$ and $f_{i\lambda}^{\pm}$ again filling factors.

IV. NICKEL DROPLET DIFFUSION ON GRAPHENE

Details of simulations. To investigate the size dependence of liquid cluster diffusion on graphene, a prototype crystalline membrane, we performed six simulations for clusters containing $N = 19, 38, 92, 147, 276$, and 405 Ni atoms, initially positioned in the middle of a $71.3 \times 72.4 \text{ \AA}^2$ graphene sheet containing 1972 C atoms. Periodic boundary conditions were applied in both directions parallel to the sheet. In contrast to previous work,⁶² the substrate was not taken static, but the MC displacement trials were applied randomly to both Ni and C atoms. A Metropolis acceptance rule was used. The temperature was taken equal to 2000 K, which is close to the Ni bulk melting temperature, $T_m = 2010 \text{ K}$, according to our model, but well above the melting temperatures of all clusters considered here.⁶⁷ Indeed, during a first run at the given temperature melting of the clusters took place in all cases. Instead, the graphene substrate did not melt, in agreement with the recently estimated melting temperature of 4900 K for graphene.⁶⁸ For each cluster size, the simulation consisted of 2.5×10^7 MC cycles. One cycle corresponds to, on average, one trial displacement per atom. In contrast to single-particle (self-)diffusion in a bulk phase, where the statistics is collected by averaging over all the particles, here we have just a single cluster and sufficient statistics has to be collected by running long simulations (see below).

To investigate the growth process in terms of Eq. (1), we also performed a simulation of the growth of liquid Ni clusters on graphene at 2000 K, starting from an initial configuration with 400 Ni atoms randomly distributed on a graphene sheet of $123.0 \times 123.5 \text{ \AA}^2$ containing 5800 carbon atoms.

Ni-graphene adhesion. To obtain information on the adhesion of Ni with graphene according to our TBFMA model, we investigated the low-temperature energetics of several reference structures.

For a monolayer of Ni on graphene, the adhesive energy is equal to -0.25 eV per Ni atom, the optimal geometry being that with all Ni atoms positioned above the centers of the hexagons of the graphene substrate. Adding more layers, forming a Ni slab with the (111)-face in contact with the graphene substrate, the adhesive energy reduces from -0.078 to -0.055 to -0.024 eV per Ni interface atom for two, three, and more than three layers, respectively. This weak Ni bulk-on-graphene adhesion, in spite of the almost perfect lattice matching of the Ni-(111) surface with the graphene substrate, is in agreement with DFT calculations.^{69,70} For clusters with numbers of atoms ranging between 55 and 201 atoms, the cohesive energies were found to vary between -0.1 and -1.2 eV per Ni interface atom, depending on the shape of the cluster, the Ni-interface orientation, and the size of the clusters, the adhesion being stronger for small clusters.

These results show that there is a weak to moderate chemical interaction between Ni and the graphene substrate. They are indicative for the nature and magnitude of the Ni-graphene interaction, although the adhesion for liquid clusters can be expected to be weaker than for solid clusters.

Analysis of the simulations. Our MC ‘‘time’’ unit τ was chosen to be equal to 500 MC cycles. Assuming that MC ‘‘time’’ is proportional to real time for not-too-short time scales, the real (physical) time interval t per MC ‘‘time’’ unit τ is

equal to $t = D_{MC}\tau/D$, where $D_{MC}\tau$ is the mean squared center-of-mass displacement (MSD) of the cluster per MC “time” unit τ and D is the diffusion constant in real units. Then, for normal diffusion in 2D, Einstein’s Brownian motion formula tells us that

$$\langle \Delta R^2(n) \rangle = 4D_{MC}\tau n, \quad (34)$$

where $\langle \Delta R^2(n) \rangle$ is the average MSD of the cluster after n MC “time” units, defined as

$$\begin{aligned} \langle \Delta R^2(n) \rangle &= \frac{1}{M_n} \sum_{m=0}^{M_n-1} \Delta R_m^2(n) \\ &= \frac{1}{M_n} \sum_{m=0}^{M_n-1} [R(m+n) - R(m)]^2, \end{aligned} \quad (35)$$

where $M_n = M - n + 1$, with M the total MC simulation “time” and where we defined $R_m(n) = R(m+n) - R(m)$. We corrected for substrate motion defining

$$R(n) = R_{cl}(n) - R_{gr}(n) - [R_{cl}(0) - R_{gr}(0)], \quad (36)$$

where R_{cl} and R_{gr} represent the cluster and graphene center of mass positions, respectively. Typically, the “time” interval over which Eq. (34) can be verified reliably is much smaller than the total simulation “time” M due to the lack of statistics for large “times” within the interval $[0, M]$. So, before plotting the MSD versus n , we first investigated the statistics by calculating the average MSD distribution function, which we formally define as

$$\rho_{MC}(\Delta R^2; n) = \frac{1}{\pi M_n} \sum_{m=0}^{M_n-1} \delta[\Delta R^2 - \Delta R_m^2(n)] \quad (37)$$

for a given MC “time” n , where δ is the Kronecker δ function, and the prefactor $1/\pi$ normalizes the 2D space integral of ρ_{MC} to one. For normal diffusion, $\rho_{MC}(\Delta R^2; n)$ should correspond to the analytical solution of the diffusion equation $\partial\rho/\partial t = D\nabla_r^2\rho(r)$ in 2D, which for the initial condition of a particle placed at the origin $\mathbf{r} = 0$ at $t = 0$ is given by

$$\rho(\mathbf{r}, t) = \rho(r^2, t) = \frac{1}{4\pi Dt} \exp\left(-\frac{r^2}{4Dt}\right). \quad (38)$$

This solution, also known as the diffusion propagator, gives the probability that the particle has moved over a distance r within the time interval t . Hence, the statistics of our simulation can be checked by calculating $\rho_{MC}(\Delta R^2; n)$ for a given MC “time” n and compare it to the analytical shape $(A/\pi)\exp(-A\Delta R^2)$ of Eq. (38). Typically, when n is a large fraction of the total simulation “time,” M , statistics will be poor and ρ_{MC} will not have converged to the analytical shape.

Results. To check the statistics for our single cluster diffusion simulations, we plotted the MSD distribution functions $\rho_{MC}(\Delta R^2; n)$ as a function of ΔR^2 for a given, fixed MC “time” interval n . Examples are given in Fig. 7 for the cluster with 92 atoms for four different “times” n . The dashed lines in the graphs represent a best fit of the analytical form $(A/\pi)\exp(-A\Delta R^2)$ with only one fitting parameter $A = 1/(4D)$. For small “time” intervals n , $\rho_{MC}(\Delta R^2; n)$ follows closely the fit, indicating good statistics, while for the largest “time” interval it deviates considerably indicating

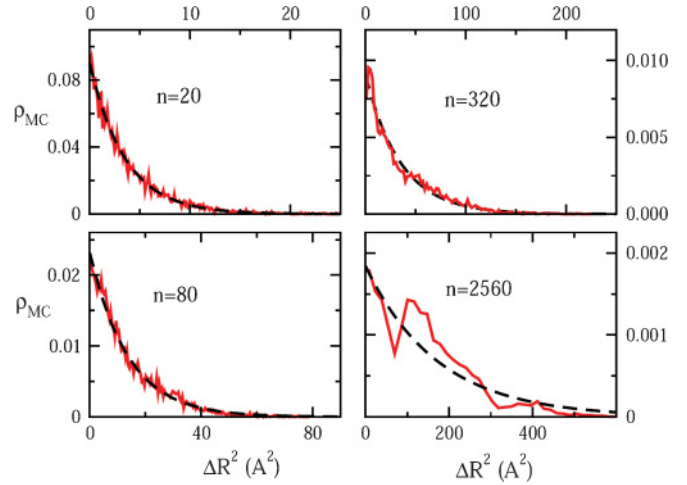


FIG. 7. (Color online) The mean squared displacement distribution function from MC simulation, $\rho_{MC}(\Delta R^2)$ (solid lines), and the best fitting analytical solution (38) (dashed lines) for different “time” intervals n , as indicated in the graphs. These results are for the Ni cluster with 92 atoms.

poor statistics, due to the reduced number of contributions to the sum in Eq. (37).

The results for the MSD distribution functions for various “time” intervals and the six clusters indicated that we can expect reliable values for the MSD as a function of n for “time” intervals up to (at least) $n = 100$, which is indeed confirmed by Fig. 8. Apart from a relatively small initial “time” interval this figure shows a linear relationship between ΔR^2 and n , allowing for a straightforward determination of the MSD per MC “time” unit, $D_{MC}\tau$, for each cluster. Subsequently plotting $D_{MC}\tau$ as a function of N in a logarithmic plot (see inset of Fig. 8) shows a power law behavior $D_{MC}\tau \propto N^{-\alpha}$ with an exponent equal to $\alpha = 0.645$, practically equal to the value $2/3$ found in Ref. 24 for solid clusters with a lattice parameter incommensurate with respect to that of the substrate. The considerably larger exponent $\alpha = 1.3$ found for a liquid cluster on a rigid, amorphous substrate in Ref. 62 might be attributed to the observed stick-and-roll diffusion mechanism. We visually checked for rolling by marking the atoms at one side of the cluster (the one with 92 Ni atoms) with a different color and following these atoms in successive MC snapshots. After only a few MC “time” intervals the marked atoms were distributed almost randomly throughout the cluster while the cluster as a whole had hardly moved. This suggests that the diffusion of the clusters does not proceed by rolling in our case. The difference in “time” scale for cluster diffusion and that of atomic self-diffusion inside the cluster is also demonstrated by the average MSD as a function of n for atomic diffusion shown by the dotted line in Fig. 8. This self-diffusion curve was determined for the biggest cluster with 405 Ni atoms by initially selecting all atoms inside a spherical region around the center of the cluster and following the average MSD only for these atoms to limit the effects of the cluster boundaries for some “time”. Indeed, for large “time” scales we found that the MSD versus n curve starts to fluctuate around a constant value due to the finite cluster size, but for smaller “time” scales the linear MSD versus n behavior was

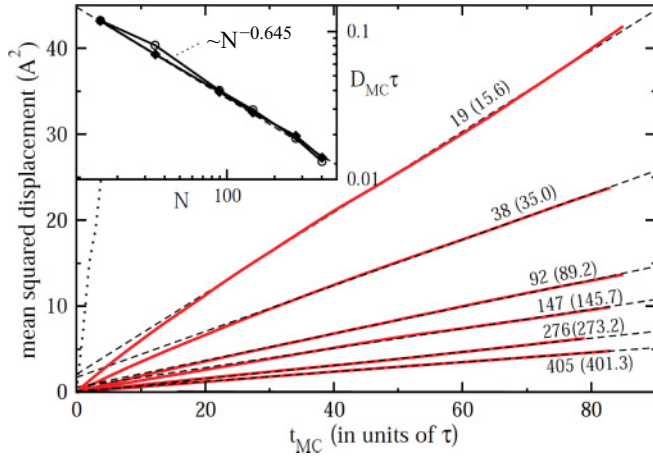


FIG. 8. (Color online) The mean squared displacement (MSD) as a function of MC “time” from the MC simulations (red solid lines) for the six different clusters as indicated by the total number of Ni atoms and the average number of atoms in the Ni cluster during the simulation (number in parentheses). We note that at the give temperature Ni atoms can detach from the cluster and eventually rejoin the cluster at a later “time.” The dashed line gives the best linear fit. The dotted line gives the MSD for atomic self-diffusion inside the cluster with 405 atoms. The inset gives the MSD per MC “time” unit, $D_{MC}\tau$, as a function of the average number of atoms inside the cluster using logarithmic scales obtained from the slopes in the main figure (solid diamonds) and from the best fit of $\rho_{MC}(\Delta R^2)$ using the analytical solution (38) (open circles). The dashed line in the inset gives the best fitting power law resulting in an exponent $\alpha = 0.645$.

recovered, as shown in Fig. 8, allowing for the determination the atomic MSD per MC “time” unit, $D_{MC,at}\tau$. As a result we find that, at 2000 K, the atomic self-diffusion is more than two orders of magnitude faster than the cluster diffusion for the cluster with 405 atoms. Using this ratio from our MC simulations and the literature value $D_{at} = 7.0 \cdot 10^{-5} \text{ cm}^2/\text{s}$ for the atomic self-diffusion constant,⁷¹ we obtain a cluster diffusion constant of $D_{405} = 5.7 \cdot 10^{-7} \text{ cm}^2/\text{s}$, comparable to the experimentally found, large cluster diffusion constant of the order of $10^{-8} \text{ cm}^2/\text{s}$ for nonepitaxially oriented gold and antimony clusters on graphite.^{51,52} This large diffusion constant suggests a mechanism dominated by random motion of the whole cluster rather than by single-atom events, although the latter is present as well. We note that in the above analysis, we tacitly made the assumption that the real time per MC “time” unit is the same for both diffusion processes; that is, we assumed that $D_{MC,at}\tau/D_{at} = D_{MC}\tau/D$, which for the present rough estimation is reasonable.

Our simulation of the growth process of liquid Ni clusters on graphene is illustrated in Fig. 9. The snapshots in panels (b) and (c) of this figure are separated by only a limited number of MC “time” units during which the four clusters in the upper right corner have merged to two clusters, which suggests the cluster coalescence represents an important contribution to the growth process. We also see single Ni atoms, detached from the cluster, diffusing on the graphene surface, demonstrating the presence of Oswald ripening. Note the apparently much larger mobility of the single atoms than that of the clusters by comparing again the images of Figs. 9(b) and 9(c). Finally,

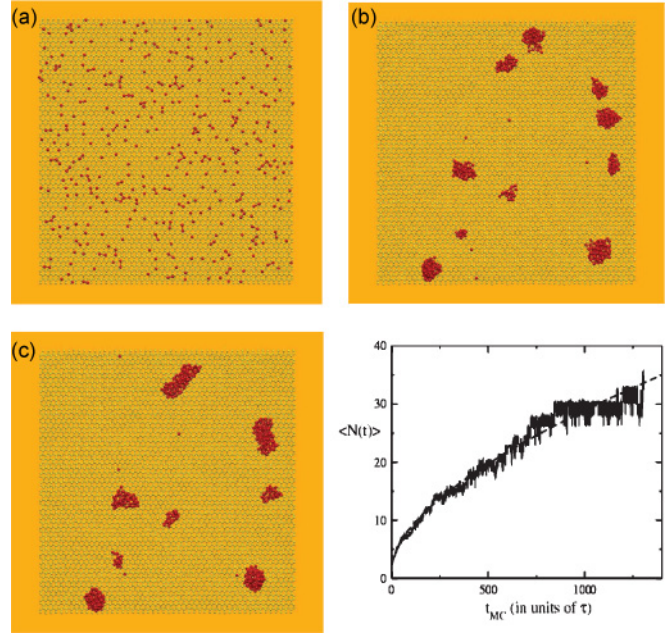


FIG. 9. (Color online) Snapshots of the simulation of the liquid droplet growth on graphene starting from randomly deposited Ni atoms (a). The snapshots (b) and (c), separated by only a limited number of MC “time” units, clearly shows the occurrence of cluster coalescence. Graph (d) gives the average cluster size $\langle N(t) \rangle$ (in number of atoms) as a function of the MC “time” t_{MC} .

the evolution of the average cluster size, $\langle N(t) \rangle$, is shown in Fig. 9(d), and compared with a best fit of the form $N_0 + K_{CC}t^{3/5} + K_{OR}t^{3\beta}$ from Eq. (1) with $\alpha = 2/3$ (dashed line). This good agreement could only be obtained by assuming a value for K_{OR} much smaller than that for K_{CC} , which implies that the growth process is almost completely dominated by cluster coalescence for the “time” scales here considered.

V. SUMMARY, CONCLUSIONS

We have presented an analytical description of TBFMA. While the TBFMA model can be considered as a next step beyond the SMA model, it is, in fact, closer to the classical TB model of which it contains the essential physics. Important implications and technical details are discussed, including, for example, an overview of the shapes of the local densities of states possible within the FMA, and the analytical expressions for the relevant integrals, obtained by applying and elaborating the general solution in Ref. 66 to the FMA. These and several other important ingredients provide the basis for a very efficient implementation of the FMA model in a MC simulation code, which allows for a simulation speed approaching that of the simpler models, based on SMA, to within one order of magnitude and which scales linearly with the system size.

Due to the possible discontinuities in the derivatives of the energy, mentioned in Sec. III B, constructing a rigorous MD implementation is not a straightforward task. We are currently working on an MD version of the model.

Our MC implementation of the TBFMA model allowed us to simulate the diffusion and growth of Ni liquid droplets

on a graphene sheet. Despite the absence of a true time scale in MC simulation, an analysis of our simulations confirms that the MC “time,” taken equal to the number of MC cycles, can be assumed to be proportional to the real time for not-too-short time scales, as has also been demonstrated previously.⁴⁵ Simulation of the single droplet diffusion for different sizes of the droplet revealed a power law behavior of the diffusion constant $D_{MC} \propto N^{-\alpha}$ with $\alpha = 0.645$, very close to the value $\alpha = 2/3$ found earlier for solid clusters with an incommensurate matching to the substrate.⁶⁰ As in the latter case, the main diffusion mechanism is the random motion of the whole cluster, giving rise to a much faster diffusion (10^{-7} cm²/s) than the diffusion dominated by single-atom events (10^{-17} cm²/s). Our exponent α is different from the value $\alpha = 1.3$ found for a liquid cluster on an amorphous, rigid surface, where the diffusion was shown to proceed via a stick-and-roll mechanism⁶² not observed in our

simulations. These facts are likely to explain the different exponents.

The exponent $\alpha = 2/3$ for the size dependence of the diffusion constant gives rise to a contribution proportional to $t^{3/5}$ in the growth of the average cluster size by coalescence in an ensemble of clusters on a 2D substrate. Our simulation of such a cluster growth process on a graphene sheet is well described by the law $t^{3/5}$ and suggests that cluster coalescence is by far the dominant process for the “time” scale and system size considered here, which did not allow us to see the crossover to a regime where Oswald ripening becomes the dominant process.

ACKNOWLEDGMENT

We thank PAN-H ANR (Mathysse) for support and Guy Tréglia for useful feedback.

-
- ¹F. H. Stillinger and T. A. Weber, *Phys. Rev. B* **31**, 5262 (1985).
²J. F. Justo, M. Z. Bazant, E. Kaxiras, V. V. Bulatov, and S. Yip, *Phys. Rev. B* **58**, 2539 (1998).
³N. A. Marks, *Phys. Rev. B* **63**, 035401 (2000).
⁴M. Finnis and J. Sinclair, *Philos. Mag. A* **50**, 45 (1984).
⁵M. I. Baskes, *Phys. Rev. Lett.* **59**, 2666 (1987).
⁶M. I. Baskes, J. S. Nelson, and A. F. Wright, *Phys. Rev. B* **40**, 6085 (1989).
⁷F. Cleri and V. Rosato, *Phys. Rev. B* **48**, 22 (1993).
⁸J. Cai and J. S. Wang, *Phys. Rev. B* **64**, 035402 (2001).
⁹J. Tersoff, *Phys. Rev. Lett.* **56**, 632 (1986).
¹⁰J. Tersoff, *Phys. Rev. B* **38**, 9902 (1988).
¹¹D. W. Brenner, *Phys. Rev. B* **42**, 9458 (1990).
¹²D. W. Brenner, O. A. Shenderova, J. A. Harrison, S. J. Stuart, B. Ni, and S. B. Sinnott, *J. Phys. Condens. Matter* **14**, 783 (2002).
¹³A. C. T. van Duin, S. Dasgupta, F. Lorant, and W. A. Goddard III, *J. Phys. Chem. A* **105**, 9396 (2001).
¹⁴A. C. T. van Duin, A. Strachan, S. Stewman, Q. Zhang, X. Xu, and W. A. Goddard III, *J. Phys. Chem. A* **3803**, 9396 (2003).
¹⁵J. H. Los and A. Fasolino, *Phys. Rev. B* **68**, 024107 (2003).
¹⁶J. H. Los, L. M. Ghiringhelli, E. J. Meijer, and A. Fasolino, *Phys. Rev. B* **72**, 214102 (2005).
¹⁷D. G. Pettifor, *Phys. Rev. Lett.* **63**, 2480 (1989).
¹⁸D. G. Pettifor and I. I. Oleinik, *Phys. Rev. B* **59**, 8487 (1999).
¹⁹I. I. Oleinik and D. G. Pettifor, *Phys. Rev. B* **59**, 8500 (1999).
²⁰D. G. Pettifor and I. I. Oleinik, *Phys. Rev. Lett.* **84**, 4124 (2000).
²¹R. Drautz, D. A. Murdick, D. Nguyen-Manh, X. Zhou, H. N. G. Wadley, and David G. Pettifor, *Phys. Rev. B* **72**, 144105 (2005).
²²D. A. Murdick, X. W. Zhou, H. N. G. Wadley, D. Nguyen-Manh, R. Drautz, and D. G. Pettifor, *Phys. Rev. B* **73**, 045206 (2006).
²³Volker Kuhlmann and Kurt Scheers Schmidt, *Phys. Rev. B* **76**, 014306 (2007).
²⁴M. Mrovec, M. Moseler, C. Elsässer, and A. B. P. Gumbsch, *Prog. Mater. Sci.* **52**, 230 (2007).
²⁵H. Amara, J. M. Roussel, C. Bichara, J. P. Gaspard, and F. Ducastelle, *Phys. Rev. B* **79**, 014109 (2009).
²⁶R. Haydock, V. Heine, and M. J. Kelly, *J. Phys. C* **5**, 2845 (1972).
²⁷R. Haydock, in *Solid State Physics*, edited by F. Seitz, D. Turnbull, and H. Ehrenreich, Vol. 35 (Academic Press, New York, 1980).
²⁸M. C. Desjonquères and D. Spanjaard, in *Concepts in Surface Physics*, Springer Series of Surface Science, 2nd ed., Vol. 30 (Springer-Verlag, Berlin, Heidelberg, New York, 1996).
²⁹F. Ducastelle, in *Order and Phase Stability in Alloys*, edited by F. R. de Boer and D. G. Pettifor (Elsevier Science Publishers, North-Holland, Amsterdam, 1991).
³⁰G. C. Abell, *Phys. Rev. B* **31**, 6184 (1985).
³¹D. W. Brenner, *Phys. Rev. Lett.* **63**, 1022 (1989).
³²B. J. Thijsse, *Phys. Rev. B* **65**, 195207 (2002).
³³K. Albe, K. Nordlund, and R. S. Averback, *Phys. Rev. B* **65**, 195124 (2002).
³⁴O. Hardouin-Duparc, *Philos. Mag.* **89**, 3117 (2009).
³⁵J. H. Los, C. Mottet, C. Goyhenex, and G. Tréglia (unpublished).
³⁶W. Yang, *Phys. Rev. Lett.* **66**, 1438 (1991).
³⁷X.-P. Li, R. W. Nunes, and D. Vanderbilt, *Phys. Rev. B* **47**, 10891 (1993).
³⁸G. Galli and M. Parrinello, *Phys. Rev. Lett.* **69**, 3547 (1992).
³⁹P. Ordejon, D. A. Drabold, M. P. Grumbach, and R. M. Martin, *Phys. Rev. B* **48**, 14646 (1993).
⁴⁰W. Kohn, *Phys. Rev. Lett.* **76**, 3168 (1996).
⁴¹S. Goedecker and L. Colombo, *Phys. Rev. Lett.* **73**, 122 (1994).
⁴²S. Goedecker, *Rev. Mod. Phys.* **71**, 1085 (1999).
⁴³L. Colombo, *Rivista del Nuovo Cimento* **28**, 1 (2005).
⁴⁴C. Noguera, J. Godet, and J. Goniakowski, *Phys. Rev. B* **81**, 155409 (2010).
⁴⁵H. E. A. Huitema and J. P. van der Eerden, *J. Chem. Phys.* **110**, 3267 (1999).
⁴⁶I. M. Lifshitz and V. V. Slyozov, *J. Phys. Chem. Solids* **19**, 35 (1961).
⁴⁷C. Wagner, *Z. Elektrochem.* **65**, 581 (1961).
⁴⁸D. Kashchiev, *Surf. Sci.* **55**, 477 (1976).
⁴⁹G. L. Kellogg, *Phys. Rev. Lett.* **73**, 1833 (1994).
⁵⁰J. -M. Wen, S. -L. Chang, J. W. Burnett, J. W. Evans, and P. A. Thiel, *Phys. Rev. Lett.* **73**, 2591 (1994).
⁵¹L. Bardotti, P. Jensen, A. Hoareau, M. Treilleux, and B. Cabaud, *Phys. Rev. Lett.* **74**, 4694 (1995).

- ⁵²L. Bardotti *et al.*, *Surf. Sci.* **367**, 267 (1996).
- ⁵³K. Morgenstern, G. Rosenfeld, B. Poelsema, and G. Comsa, *Phys. Rev. Lett.* **74**, 2058 (1995).
- ⁵⁴A. F. Voter, *Phys. Rev. B* **34**, 6819 (1986).
- ⁵⁵J. M. Soler, *Phys. Rev. B* **50**, 5578 (1994).
- ⁵⁶Clinton De W. VanSiclen, *Phys. Rev. Lett.* **75**, 1574 (1995).
- ⁵⁷S. V. Khare, N. C. Bartelt, and T. L. Einstein, *Phys. Rev. Lett.* **75**, 2148 (1995).
- ⁵⁸D. S. Sholl and R. T. Skodje, *Phys. Rev. Lett.* **75**, 3158 (1995).
- ⁵⁹J. M. Soler, *Phys. Rev. B* **53**, R10540 (1996).
- ⁶⁰P. Deltour, J. L. Barrat, and P. Jensen, *Phys. Rev. Lett.* **78**, 4597 (1997).
- ⁶¹V. N. Antonov, J. S. Palmer, A. S. Bhatti, and J. H. Weaver, *Phys. Rev. B* **68**, 205418 (2003).
- ⁶²F. Celestini, *Phys. Rev. B* **70**, 115402 (2004).
- ⁶³L. J. Lewis, P. Jensen, N. Combe, and J.-L. Barrat, *Phys. Rev. B* **61**, 16084 (2000).
- ⁶⁴J. C. Slater and G. F. Koster, *Phys. Rev.* **94**, 1498 (1954).
- ⁶⁵J. P. Gaspard (private communication).
- ⁶⁶G. Allan, M. C. Desjonqueres, and D. Spanjaard, *Solid State Commun.* **50**, 401 (1984).
- ⁶⁷J. H. Los and R. J. M. Pellenq, *Phys. Rev. B* **81**, 064112 (2010).
- ⁶⁸K. V. Zakharchenko, A. Fasolino, J. H. Los, and M. I. Katsnelson, *J. Phys. Condens. Matter* **23**, 202202 (2011).
- ⁶⁹D. J. Klink II, S. Wilke, and L. J. Broadbelt, *J. Catal.* **178**, 540 (1998).
- ⁷⁰M. Vanin, J. J. Mortensen, A. K. Kelkkanen, J. M. Garcia-Lastra, K. S. Thygesen, and K. W. Jacobsen, *Phys. Rev. B* **81**, 081408(R) (2010).
- ⁷¹F. J. Cherne, M. I. Baskes, and P. A. Deymier, *Phys. Rev. B* **65**, 024209 (2001).